Available online at www.sciencedirect.com

ScienceDirect

Journal of Ocean Engineering and Science 2 (2017) 61–75

www.elsevier.com/locate/joes

Original Article

Predicting scour beneath subsea pipelines from existing small free span depths under steady currents

Jun Y. Lee[a,*], Jasmin McInerney[b], Remo Cossu[c,a], Zhi Q. Leong[a], Alexander L. Forrest[b,a]

[a] *National Centre for Maritime Engineering and Hydrodynamics, Australian Maritime College, University of Tasmania, 1 Maritime Way, Newnham Tasmania 7248, Australia*

[b] *Department of Civil and Environmental Engineering, University of California – Davis, 1 Shields Avenue, Davis, CA 95616, United States of America*

[c] *School of Civil Engineering, University of Queensland, St Lucia Queensland 4072, Australia*

Received 5 October 2016; received in revised form 9 February 2017; accepted 3 March 2017
Available online 18 March 2017

Abstract

An equation was developed to predict current-induced scour beneath subsea pipelines in areas with small span depths, *S*. Current equations for scour prediction are only applicable to partially buried pipelines. The existence of small span depths (i.e. $S/D < 0.3$) are of concern because the capacity for scour is higher at smaller span depths. Furthermore, it is impractical to perform rectification works, such as installing grout bags, under a pipeline with a small *S*/*D*. Full-scale two-dimensional computational fluid dynamics (CFD) simulations were performed using the Reynolds-averaged Navier–Stokes approach and the Shear stress transport k–ω turbulence model. To predict the occurrence of scour, the computed maximum bed shear stress beneath the pipe was converted to the dimensionless Shields parameter, and compared with the critical Shields parameter based on the mean sediment grain size. The numerical setup was verified, and a good agreement was found between model-scale CFD data and experimental data. Field data were obtained to determine the mean grain size, far field current velocity and to measure the span depths along the surveyed pipe length. A trend line equation was fitted to the full-scale CFD data, whereby the maximum Shields parameter beneath the pipe can be calculated based on the undisturbed Shields parameter and *S*/*D*.

Keywords: Sediment scour; Subsea pipelines; Small span depths; Steady currents.

1. Introduction

Subsea pipelines transport oil or natural gas across vast distances along the seabed. The marine sediment beneath the pipeline can be eroded by current and/or wave action. Sediment erosion, commonly referred to as scour, can lead to free span formation in the vicinity of a subsea pipeline [1]. However, the time required to reach an equilibrium scour depth in the field is much longer than storm periods [2]. Thus, a pipeline may have multiple spans with small depths (defined as $S < 0.3D$ in this paper) upon experiencing strong currents. Furthermore, initial free spans can also be present when a pipeline is laid on an uneven seabed. Scour can occur when flow is accelerated underneath the pipe, which will widen and deepen existing free spans. Free spans can be permanent [3] and rectification works are often required (e.g. installing grout bags), where the risk of vortex-induced vibration causing fatigue is high. In addition, installing grout bags, which are relatively large, under a pipeline with a small span depth is often impractical. Therefore, it is necessary to predict the occurrence of scour beneath a pipeline from existing small span depths.

The mechanics of scour beneath an initially buried pipe under steady currents has been extensively studied using laboratory experimentation [4–7]. Initially, when there is a flow-induced pressure difference between the upstream and downstream sides of a pipe, water can flow through the voids between the sediment particles beneath the pipe (i.e. seepage flow). Eventually, a mixture of water and sediment will be discharged at the immediate downstream side of the pipe (i.e.

* Corresponding author at: Locked Bag 1395, Launceston Tasmania 7250, Australia.
E-mail address: jylee4@utas.edu.au (J.Y. Lee).

http://dx.doi.org/10.1016/j.joes.2017.03.001

piping) [4]. This is followed by a 'jet period' (i.e. tunnel scour) where sediment is syphoned underneath the pipe [5]. As more sediment is eroded, the scour hole deepens. When the scour depth exceeds the equivalent of 30% of the pipe diameter (i.e. $S/D > 0.3$), periodic vortex shedding occurs in the wake of the pipe [5,8], which leads to further erosion downstream of the pipe. Empirical relationships have been derived based on two-dimensional studies, to estimate the critical far field current velocity for scour onset around a partially buried pipe (e.g. Sumer et al. [6]), without the consideration of an existing free span depth, S.

Although laboratory experiments provide a good platform for studying the mechanics of scour, they are limited by the dimensions of the experimental facility. Scaled experiments tend to exhibit scale effects when, for example, excessive fluid viscous forces are introduced [9]. To date, although there are several models for scaling general sediment transport experiments, perfect similitude remains a physical impossibility [9]. With scaled sediment, the sediment grain size will be so small that they exhibit cohesive properties, which are not characteristic of the sediment at its full scale [10]. Having smaller sediment with cohesive properties will result in scour propagation timescales to be falsely exaggerated [11], compared to predictions via empirical formulae developed for non-cohesive sediment (e.g. Fredsøe et al. [12]). Therefore, there is a need to conduct full-scale studies.

Due to the spatial and time scales associated with studying the mechanics of scour around a full-scale pipeline, it is often logistically impractical to rely on field measurements. With some notable exceptions (e.g. Leckie et al. [13]), limited field data have been obtained and published. To address this paucity of data, numerical simulations offer a viable alternative as the simulations can be performed at full-scale. Previous numerical studies [14–18] have demonstrated that computational fluid dynamics (CFD) can be used to accurately model flow around a cylinder close to a flat bed. However, these studies did not focus on the implications of scour. Only a few studies have investigated the amplification of the seabed shear stresses resulting from the presence of the pipe [19,20]. Although a higher amplification factor suggests a higher sediment transport capacity; yet, this cannot be directly related to the prediction of scour occurring beneath a pipe. Nevertheless, direct correlation is possible via the use of the classic Shields parameter [21], which is widely used to predict the initiation of sediment transport.

We predict the maximum Shields parameter (i.e. normalised maximum bed shear stress) beneath a full-scale pipeline for a range of span depths and far field current velocities. An equation was fitted to the full-scale CFD results, which can be used to calculate the maximum Shields parameter beneath the pipeline, based on the undisturbed Shields parameter and span-depth-to-diameter ratio, S/D. The predicted maximum Shields parameter can then be compared to the critical Shields parameter for the mean sediment grain size, to predict whether scour will occur. Small span depths (i.e. $S/D < 0.3$) are of interest not only because shear stress amplification is higher at smaller depths [19], but also, performing rectification works (e.g. installing grout bags) are difficult or impractical. Therefore, it is essential to predict the occurrence of scour beneath pipelines in areas with small span depths.

2. Theoretical considerations

The Shields parameter is a dimensionless representation of the bed shear stress and is calculated using Eq. (1) [21]:

$$\theta = \frac{{u_*}^2}{\left(\frac{\rho_S}{\rho} - 1\right) g d_{50}} \tag{1}$$

where u_* is the friction velocity, which can be calculated via $u_* = (\tau/\rho)^{1/2}$ [22]; τ is the bed shear stress; ρ_s is sediment density; ρ is fluid density; g is gravitational acceleration; and, d_{50} is the mean sediment grain size. This classic parameter is widely used to predict the onset of sediment transport. When a threshold value (i.e. critical Shields parameter, θ_{cr}) is exceeded, then it is likely that sediment transport will occur. A wide range of critical Shields parameters for different mean grain sizes are available in literature (e.g. Barton et al. [23]). Furthermore, it can even be calculated using Eq. (2) from Soulsby [22]:

$$\theta_{cr} = \frac{0.30}{1 + 1.2 D_*} + 0.055\left[1 - \exp\left(-0.02 D_*\right)\right] \tag{2}$$

where D_*, which is the dimensionless form of the sediment grain size, is calculated using Eq. (3) [22]:

$$D_* = \left[\frac{g(s-1)}{\nu^2}\right]^{1/3} d_{50} \tag{3}$$

where s is the specific weight of the sediment, normalised by the specific weight of the surrounding liquid; and, ν is the kinematic viscosity of the liquid.

A few equations have been developed to predict scour onset beneath partially buried subsea pipelines. Using laboratory experiments, Sumer et al. [6] derived Eq. (4) to estimate the critical velocity for scour onset based on partially buried pipelines affected by current action:

$$U_{cr} = \sqrt{\left(0.025 \exp\left[9(e/D)^{0.5}\right]\right) \times gD(1-n)(s-1)} \tag{4}$$

where e is the embedment or burial depth; D is the external pipe diameter; and, n is sediment porosity.

Zang et al. [24] further extended this work using numerical simulations, to estimate the critical flow velocity, due to currents and/or waves, at which scour onset around a partially buried pipe is likely to occur. This is given by:

$$\frac{u_m^2}{gD(s_0 - 1)(1-n)} \geq \frac{\gamma}{\lambda_A \Delta C_{p0}} \left(1 - \exp(-0.018 KC^{1.5})\right) \tag{5}$$

where u_m is the amplitude of oscillatory velocity; s_0 is equivalent to s; γ is the contact angle for the pipe; $\lambda_A \Delta C_{p0}$ is the exit pressure gradient coefficient; and, KC is the Keulegan–Carpenter number.

The disadvantage of Eq. (4) is that it is an empirical equation based on experiments; hence, scaling can have an effect on the outcome as it is impossible to have perfect similitude

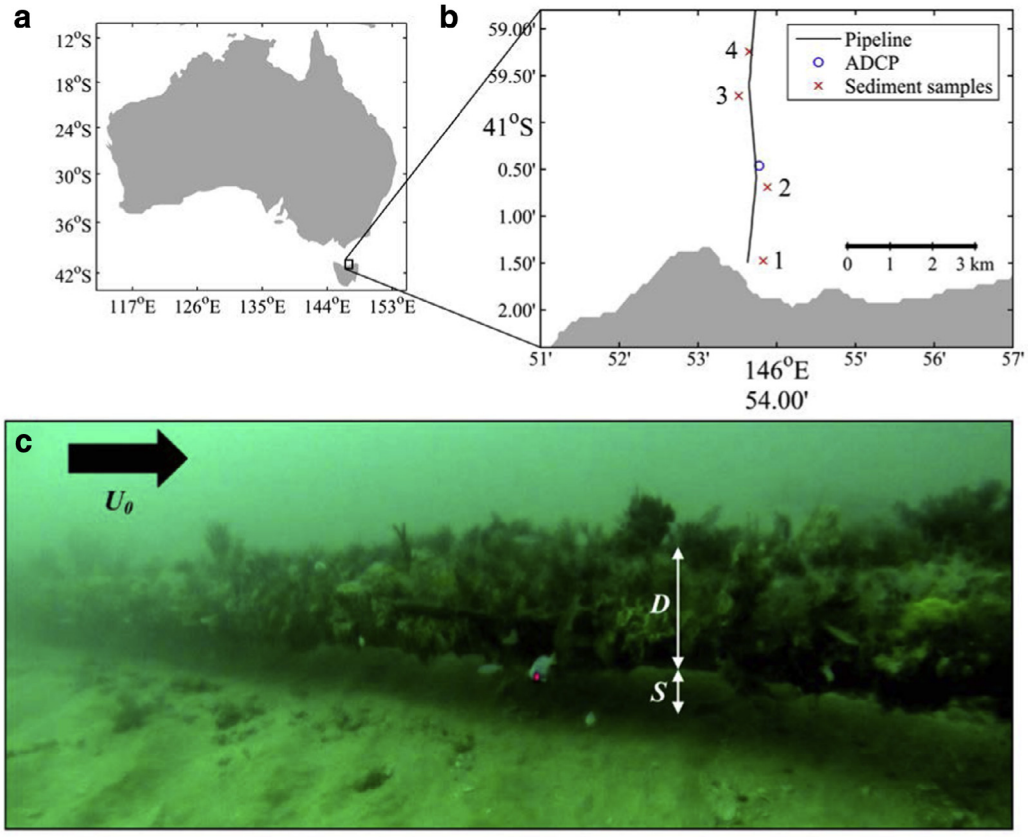

Fig. 1. (a) Surveyed site location with respect to Australia plotted using the Miller projection. (b) Location of a 5 km stretch of the Tasmanian Gas Pipeline (TGP), acoustic Doppler current profiler (ADCP) mooring and sediment sampling points. (c) Snapshot of Remotely Operated Vehicle (ROV) footage obtained while conducting a visual inspection of the TGP at several kilometres off the coast of Northern Tasmania in May 2015. The key parameters here are the span depth, S, pipe diameter, D, and the free stream velocity, U_0, which is measured at 2 m above the seabed.

[9]. While Eq. (5) is more comprehensive, it is not easily solved with λ_A and ΔC_{p0}. Furthermore, Eqs. (4) and (5) are only applicable for partially buried pipes, creating the need to model the effects of the S/D ratio. Therefore, we aim to predict the occurrence of scour beneath a pipe with a small S/D, by using the classic Shields parameter. Further details on the derivation of the equation are presented in Section 3.4.

3. Methods

The main results were obtained via numerical computations. Field measurements were obtained to provide supplementary data to perform the CFD simulations, while experimental data provide a benchmark for CFD modelling.

3.1. Field investigation

A field survey was conducted for the southernmost 5 km section of the Tasmanian Gas Pipeline (TGP), off the Northern Tasmanian coast in South Eastern Australia (Fig. 1a). The TGP transports natural gas across the Bass Strait with an offshore section over 300 km long, and is currently at an annual capacity of 47 PJ [25] (see Table 1 for the design parameters and operating conditions). Several field measurements and information extracted from [25] were used to devise the numerical test conditions. The field survey was mainly conducted to obtain the following:

- Ensemble-averaged water column velocities recorded at 50 m east of the pipeline.
- Mean grain size of the sediment in the vicinity of the surveyed site.
- Approximated maximum span depths of each span along the surveyed pipe length.

A Teledyne Sentinel V 500 kHz 4-beam Acoustic Doppler Current Profiler (ADCP) was deployed at a location 50 m east of the pipeline (Fig. 1b), where the average water depth was approximately 23 m. Key ADCP profile settings were: 25 m range, 0.50 m cell size, 50 cells and 1.0 m blanking distance. The resolution and accuracy were 0.001 and ±0.003 m/s respectively [26]. Transient water column velocity data over a period of 8 days (i.e. from 25 May 2015 4:53:38 UTC to 2 June 2015 22:28:38 UTC) was ensemble-averaged over 5-min intervals.

A total of four sediment samples were collected within safe distances from the TGP (Fig. 1b), as recommended by the pipeline operator. A Large Ekman Bottom Grab sediment sampler with dimensions of 0.23 m × 0.23 m × 0.23 m was used. The sediments were oven-dried, and subsequently,

Table 1
Design parameters and operating conditions of the Tasmanian Gas Pipeline (TGP) [25].

Parameter	Details
Pipeline length	301.6 km
External pipe diameter	355.6 mm
Pipe wall thickness	11.1 mm
Pipe wall thickness (shore crossing)	12.7 mm
Nominal concrete weighted coating	38 mm
Grade	X65
Maximum allowable operating pressure (MAOP)	15.3 MPa (g)
Offshore pipeline average design temperature	13 °C
Marine sediment type	Fine and medium grained quartzose sands
Mean grain size	0.12–0.25 mm
Current speeds during 5 year return period storms	0.30–0.79 m/s
Current speeds during 100 year return period storms	0.41–1.03 m/s

filtered through a set of sieves on a sieve shaker. The amount of sediment in each sieve was then measured to produce a particle size distribution curve for each sample. A mean particle size, d_{50}, was then estimated from the particle size distributions. The d_{50} was used to calculate the Nikuradse roughness, k_s, and subsequently, the associated bed roughness length, z_0, to be incorporated in the CFD computations. As the field data collected in this paper was relatively limited, information from [25], such as the current speeds during 100 year return period storms, was also used to devise the numerical test matrix (Table 3).

Video footage of the TGP was obtained using a SeaBotix LBV300 explorer class Remotely Operated Vehicle (ROV) (Fig. 1c). Several key parameters for this field investigation were the span depth, S, pipe diameter, D, and the free stream velocity, U_0, which is measured at 2 m above the seabed. Due to physical constraints, the lowest elevation from the seabed at which the velocity can be measured was 1.5 m. This is due to the 0.5 m clearance between the seabed and the top of the ADCP that was attached to an anchored steel frame, in addition to the 1.0 m blanking distance.

A Gavia Scientific Autonomous Underwater Vehicle (AUV) with a 500 kHz Kongsberg GeoAcoustics GeoSwath Plus interferometric sonar module was employed to produce acoustic backscatter images of the TGP and the seabed. This was done to identify and geo-reference free spans, and to estimate the maximum free span depths along the 5 km stretch of the TGP. Interferometric sonar exploits the phase of the reflected sound waves (i.e. acoustic return) and the return range, to estimate the position of the reflector (see Gostnell and Yoos [27] for further details). Further details regarding the application of acoustic backscatter imagery are presented in McInerney et al. [28]. Although a Global Positioning System (GPS) receiver is unreliable underwater [29], with a Kearfott T-24 Inertial Navigation System (INS) on board the AUV, the position drift is less than 0.1% of the distance travelled [30]. Therefore, there is a high level of confidence in the accuracy of the survey data.

3.2. Circulating water channel experiments

Flow experiments were conducted in a Circulating Water Channel (CWC) of 17.2 m in length, 5.0 m wide and 2.5 m deep, to investigate the flow velocities between a pipe and a flat boundary (highlighted in red in Fig. 2). The image of a slightly angled side view of the experimental setup (Fig. 2) was slightly distorted, especially at the edges, due to light refraction off the glass. A PVC pipe 4 m in length with an external diameter of 0.3 m and thickness of 0.005 m was elevated to 0.1 m (i.e. $S/D = 1/3$) above a 3.15 m long, 1.70 m wide and 0.003 m thick aluminium flat plate. The pipe was positioned above the centre of the flat plate, thus being 1.6 m from the leading edge of the plate (i.e. more than $5D$). The test rig was situated in the middle of the CWC and bolted to the walls.

Table 2
Test matrix for circulating water channel experiments.

Span depth, S (m)	Pipe diameter, D (m)	Inlet velocity, U_0 (m/s)	Pipe Reynolds number, Re
$D/3$	0.3	0.18	4.43×10^4
$D/3$	0.3	0.24	6.01×10^4
$D/3$	0.3	0.30	7.60×10^4
$D/3$	0.3	0.37	9.18×10^4
$D/3$	0.3	0.43	1.08×10^5
$D/3$	0.3	0.49	1.23×10^5
$D/3$	0.3	0.56	1.39×10^5

The flow velocity beneath the centreline of the pipe, at 0.035 m above the flat plate, was measured using a Sontek Acoustic Doppler Velocimeter (ADV) at a rate of 50 Hz. The ADV probe has an acoustic transmitter and three receivers, 9×10^{-8} m^3 sampling volume, 1×10^{-4} m/s resolution and an accuracy of 1% of measured velocity [31]. The ADV probe was located slightly downstream, so that the receivers are positioned at 0.05 m downstream from the vertical centreline of the pipe. This was done to ensure that the flow velocity, u_{35}, is measured within the sampling volume. Further details on ADVs are presented in Voulgaris and Trowbridge [32]. The test conditions are listed in Table 2 and each run was repeated twice. Inlet flow velocities corresponding to the pipe Reynolds numbers, Re, in the sub-critical regime ($5 \times 10^3 < Re < 2 \times 10^4$) were selected, which were observed in the field.

The average inflow velocities were determined based on a calibration curve derived prior to the experiments. During

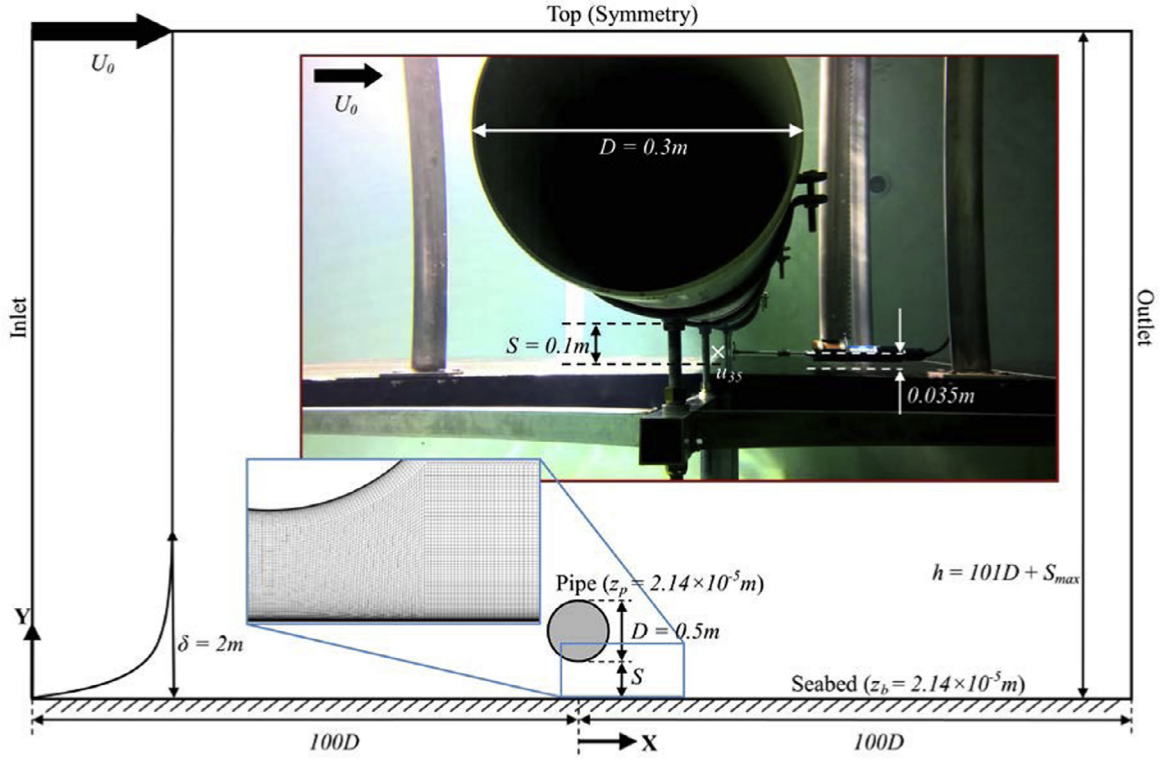

Fig. 2. Angled cross-stream view of the CWC experimental setup shown in a red box, within a schematic diagram illustrating the full-scale domain employed for CFD computations. A close-up view of the mesh between the pipe and the seabed, for $S/D = 0.28$, is shown in a blue box. (For interpretation of the references to colour in this figure legend, the reader is referred to the web version of this article.)

the calibration process, the ADV was placed several metres upstream of the pipe to measure flow velocities at a range of pump revolution speeds. Inlet flow velocities were not measured upstream during the actual experiments to minimise wake effects downstream of the ADV, which will affect the flow measurements beneath the pipe. It is also worth noting that due to physical limitations, it was not possible to directly measure the shear velocity, u_*, or have a smaller span depth.

3.3. Numerical computations

There are three stages with regards to computational fluid dynamics (CFD) modelling. Firstly, verification was completed to estimate the numerical uncertainty. Secondly, comparisons between model-scale CFD and experimental data from the CWC experiments and Jensen et al. [33] were conducted. Lastly, a full-scale computational domain was employed, where an external pipe diameter of 0.5 m was used, representing the TGP. A trend line equation was then fitted to the full-scale data, which can be used to predict the occurrence of scour beneath the TGP in areas with existing small span depths.

3.3.1. Simulation setup

A commercial CFD solver, STAR-CCM+ V10, was used to solve the incompressible Navier–Stokes equations via the finite volume method; the interested reader is referred to Tu et al. [34] for further details. The Reynolds-Averaged Navier Stokes (RANS) approach was used to compute the mean flow velocity profile beneath the pipe, and all cases are within the bound of $S/D < 0.3$, where periodic vortex shedding in the wake of the pipe was not observed in previous experiments [5,8]. The shear stress transport (SST) k–ω turbulence model [35] was employed to model the Reynolds stress term in the Reynolds-averaged Navier–Stokes equation. A comparison of several turbulence models showed that the SST k–ω model is appropriate for modelling flow around a wall-mounted circular cylinder via good agreement with experimental measurements [15].

A large two-dimensional (2D) computational domain was employed for the simulation cases (Fig. 2). A block-structured approach was adopted to generate the computational grids (a sample grid is highlighted in blue). As the seabed appeared to be relatively flat based on the ROV footage (Fig. 1c), it was assumed, for simplicity, to be flat in the CFD simulations as well. For the full-scale simulations, the inlet boundary is set to $100D$ upstream of the pipe, to ensure that the flow is fully developed when it encounters the pipe. The outlet boundary distance is also set to $100D$ to avoid artificial blockage effects with a sufficiently large domain. Zang et al. [24] demonstrated that the effects of the water depth on the flow field around the pipe diminish over $20D$. Hence, the water depth, h, was set to a large value, where $h = 101D + S_{max}$; $S_{max} = 0.28D$. h also remained constant for all cases to maintain the far field conditions (e.g. inlet velocity profile) for different values of S.

Table 3
Parameters considered for the main numerical simulations performed at full-scale.

Span depth ratio, S/D	Pipe diameter, D (m)	Seabed roughness, z_b (m)	Pipe roughness, z_p (m)	Far field current velocity, U_0 (m/s)
0.07	0.5	2.14×10^{-5}	2.14×10^{-5}	0.05
0.07	0.5	2.14×10^{-5}	2.14×10^{-5}	0.10
0.07	0.5	2.14×10^{-5}	2.14×10^{-5}	0.20
0.07	0.5	2.14×10^{-5}	2.14×10^{-5}	0.40
0.07	0.5	2.14×10^{-5}	2.14×10^{-5}	0.80
0.14	0.5	2.14×10^{-5}	2.14×10^{-5}	0.05
0.14	0.5	2.14×10^{-5}	2.14×10^{-5}	0.10
0.14	0.5	2.14×10^{-5}	2.14×10^{-5}	0.20
0.14	0.5	2.14×10^{-5}	2.14×10^{-5}	0.40
0.14	0.5	2.14×10^{-5}	2.14×10^{-5}	0.80
0.14	0.5	1.00×10^{-5}	2.14×10^{-5}	0.10
0.14	0.5	1.00×10^{-6}	2.14×10^{-5}	0.10
0.14	0.5	2.14×10^{-5}	1.00×10^{-5}	0.10
0.14	0.5	2.14×10^{-5}	1.00×10^{-6}	0.10
0.28	0.5	2.14×10^{-5}	2.14×10^{-5}	0.05
0.28	0.5	2.14×10^{-5}	2.14×10^{-5}	0.10
0.28	0.5	2.14×10^{-5}	2.14×10^{-5}	0.20

Eq. (6) [22] was used to define the velocity profile at the inlet boundary:

$$U(z) = \frac{u_*}{\kappa}\ln\left(\frac{z}{z_0}\right) \tag{6}$$

where $U(z)$ is the velocity profile; $\kappa = 0.40$ is the von Kármán constant [22]; z is the elevation from the seabed; the boundary layer thickness, δ, is set to 2 m for all cases; and, z_0 is the bed roughness length. Therefore, at $z \geq 2$ m, the inlet velocity will be equal to the free stream velocity, U_0. Previous studies [14,24] have demonstrated that, although the dimensionless inlet boundary layer thickness, δ/D, has a significant effect on the flow field around the pipe, it diminishes when $\delta/D > 1$ [14]. Thus, as $\delta = 2$ m in this case, which means that $\delta/D = 4$, its effects are negligible; moreover, it is also expected to be large in the field. As the average water temperature recorded by the ADCP was 14 °C, a seawater density, ρ, of 1026.236 kg m^{-3} and fluid kinematic viscosity, ν, of 1.2205×10^{-6} m^2/s was used [36]. It is worth noting that, while modelling the experiments, the distance of the inlet boundary is set to match the CWC experiments and that of Jensen et al. [33], to account for the bed boundary layer thickness.

The bed roughness length was estimated via a combination of the following assumptions: (1) the flow is hydrodynamically rough [22], and hence $z_0 = k_s/30$, where k_s is the Nikuradse roughness; and subsequently, (2) $k_s = 2.5d_{50}$ (see Soulsby and Humphery [37] for further details). Assuming that the mean particle size is 0.257 mm, $z_0 \approx 2.14\times10^{-5}$ m, which is close to $z_0 = 2.08\times10^{-5}$ m for $d_{50} = 0.25$ mm with reference to Det Norske Veritas [38], and hence is reasonable. As for modelling the CWC and Jensen et al.'s [33] experiments, the seabed was defined as a smooth boundary because a smooth bottom was used in the experiments.

Surface roughness was taken into account for both the seabed and the pipe in the CFD computations. The pipe roughness length, z_p, was assumed to be the same as the bed roughness length (i.e. $z_p \approx 2.14\times10^{-5}$ m), which represents an un-coated steel pipe [39] for simplicity. This does not represent the effects of marine growth on the pipe. Nevertheless, previous experimental investigations suggest that the pipe roughness pose an insignificant influence on the scour process [1].

The test conditions for the main full-scale CFD simulations are listed in Table 3, corresponding to the Tasmanian Gas Pipeline with an external diameter of 0.5 m. Three span-depth-to-diameter ratios, S/D, were investigated where small S/D ratios (i.e. $S/D < 0.3$) were of interest. The lower end of the velocity range corresponds to the mean flow velocity recorded by the ADCP, which translates to a very low undisturbed Shields parameter (i.e. $\theta_\infty < \theta_{cr}$). The middle range corresponds to the maximum velocity recorded by the ADCP, while the higher end corresponds to the current speeds occurring during 100 year return period storms [25].

Ultimately, the main aim of performing the CFD simulations was to compute the maximum bed shear stresses beneath the TGP, τ_{max}, at different span depths, S, and current velocities, U_0. The maximum Shields parameter beneath the pipe, θ_{max}, was calculated based on τ_{max}, using Eq. (1). θ_{max} was then compared against the critical Shields parameter, θ_{cr}, based on the mean grain size, d_{50}, to estimate whether scour will occur beneath the TGP. In STAR-CCM+ V10, the bed shear stress, τ, is calculated from the friction velocity, u_*, via the assumption that $u_* \equiv (\tau/\rho)^{1/2}$ [40]. u_* is termed as the 'reference velocity' and ρ is fluid density. When the SST k–ω turbulence model is selected, STAR-CCM+ calculates the reference velocity, u_*, as follows:

$$u^* = \sqrt{g\nu u/y + (1-g)\beta^{*1/2}k} \tag{7}$$

where the blending function, $g = \exp(-Re_y/11)$, is dependent on the wall-distance Reynolds number, Re_y, which can be calculated via $Re_y = (k)^{1/2}y/\nu$. k is turbulent kinetic energy; y is the normal distance from the wall to the centroid of the adjacent cell; ν is kinematic viscosity; u is the velocity

Table 4
Test matrix for the grid independence study.

Grid nodes on pipe	Number of cells	Span depth ratio, *S/D*	Pipe diameter, *D* (m)	Seabed roughness, z_b (m)	Pipe roughness, z_p (m)	Far field current velocity, U_0 (m/s)
200	44,860	0.14	0.5	2.14×10^{-5}	2.14×10^{-5}	0.20
400	148,758	0.14	0.5	2.14×10^{-5}	2.14×10^{-5}	0.20
800	494,306	0.14	0.5	2.14×10^{-5}	2.14×10^{-5}	0.20

parallel to the wall; and the constant, $\beta^* = 0.09$, is a default value recommended by STAR-CCM+ [40].

3.3.2. Verification and validation

Verification was performed to estimate the numerical uncertainty associated with the CFD simulations, by observing the changes in the computed results with an increase in the number of cells (i.e. spatial resolution of the grid in the x and y directions). The grid was refined by increasing the number of grid points surrounding the pipe by a factor of 2, which was followed by the adjacent grid lines and refinement around the seabed. The test conditions of the grid independence study are presented in Table 4. The maximum bed shear stress beneath the pipe, τ_{max}, was used as a reference to observe the influence of grid refinement. The generalised Richardson extrapolation method was employed to estimate the numerical error, $\delta^*_{RE_{k_1}}$ [41-45]:

$$\delta^*_{RE_{k_1}} = \frac{\varepsilon_{k_{21}}}{r_k^{p_k} - 1} \tag{8}$$

where p_k, the order of accuracy, was calculated via:

$$p_k = \frac{\ln\left(\varepsilon_{k_{32}}/\varepsilon_{k_{21}}\right)}{\ln\left(r_k\right)} \tag{9}$$

where $\varepsilon_{k_{21}}$ is the difference between τ_{max} computed using a 'fine' mesh and a 'medium' mesh; $\varepsilon_{k_{32}}$ is the difference between τ_{max} computed using a 'medium' mesh and a 'coarse' mesh; the grid refinement ratio, r_k, is the ratio of number of cells in the 'fine' mesh over the number of cells in the 'medium' mesh, thus $r_k = 3.32$. The ratio of number of cells in the 'medium' mesh over the number of cells in the 'coarse' mesh was also 3.32.

The numerical uncertainty or, more specifically, the grid uncertainty, U_G, was estimated via [41-43]:

$$U_G = \begin{cases} \left[9.6(1 - C_k)^2 + 1.1\right]\left|\delta^*_{RE_{k_1}}\right|, & |1 - C_k| < 0.125 \\ \left[2|1 - C_k| + 1\right]\left|\delta^*_{RE_{k_1}}\right|, & |1 - C_k| \geq 0.125 \end{cases} \tag{10}$$

which is valid when $C_k > 1$ [41-43]; where C_k, a correction factor, was included to account for the effects of higher-order terms, which was estimated using:

$$C_k = \frac{r_k^{p_k} - 1}{r_k^{p_{kest}} - 1} \tag{11}$$

where p_{kest} is an estimate for the theoretical order of accuracy, which was assumed to be 1 [43]. The root mean squared residuals were below 5×10^{-5} for all simulations and thus the iteration error was neglected. Furthermore, the error associated with blockage effects was also deemed to be insignificant because the computational domain was very large.

The validation uncertainty, U_V, was calculated via [42,43]:

$$U_V = \sqrt{U_G^2 + U_D^2} \tag{12}$$

where U_D is the uncertainty of the benchmark data (i.e. experimental uncertainty). When the comparison error, E, which is the difference between the experimental and numerical value, is less than the validation uncertainty, U_V, then it is safe to assume that the simulation setup is successfully validated [41-45].

3.4. Derivation of the equation for scour prediction

The undisturbed Shields parameter, θ_∞, was adopted to represent the upstream condition because, firstly, the scour rate was experimentally shown to be influenced by the undisturbed Shields parameter. As reported in Mao [5], the scour rate beneath the pipe at the early stage is higher at larger values of θ_∞. Secondly, although the influence of the undisturbed Shields parameter on the equilibrium scour depth is weak in the case of live-bed scour, its effect is significant when its value is less than the critical Shields parameter [1]. Hansen [46] and Mao [5] showed that there is a steep gradient in the equilibrium scour depth when $\theta < \theta_{cr}$. Thus, Sumer and Fredsøe [1] also stated that the effect of θ should be taken into consideration in the case of clear-water scour. Thirdly, the Shields parameter has been used for scaling laboratory experiments to investigate sediment transport for many years [47]. Finally, the undisturbed Shields parameter is a dimensionless parameter that encompasses both the local flow speed and the sediment grain size. Therefore, it is suitable to be used to represent the upstream condition.

The far field current velocity, U_0, was represented in the undisturbed Shields parameter, θ_∞, using Eq. (14), which was derived by substituting Eq. (13) into Eq. (1):

$$u_* = \frac{\kappa U_0}{\ln\left(z/z_0\right)} \tag{13}$$

$$\theta_\infty = \left[\frac{\kappa U_0}{\ln\left(z/z_0\right)}\right]^2 \times \frac{1}{\left(\frac{\rho_s}{\rho} - 1\right) g d_{50}} \tag{14}$$

where the sediment density, ρ_s, is assumed to be 2650 kg/m^3 [22]. The maximum Shields parameter, θ_{max}, which is the key parameter of interest, was calculated based on the maximum bed shear stress beneath the TGP, τ_{max}, that was computed via CFD. Thus, by fitting trend lines to the CFD data, the equation for the prediction of scour occurring beneath the TGP from existing small free span depths under steady currents

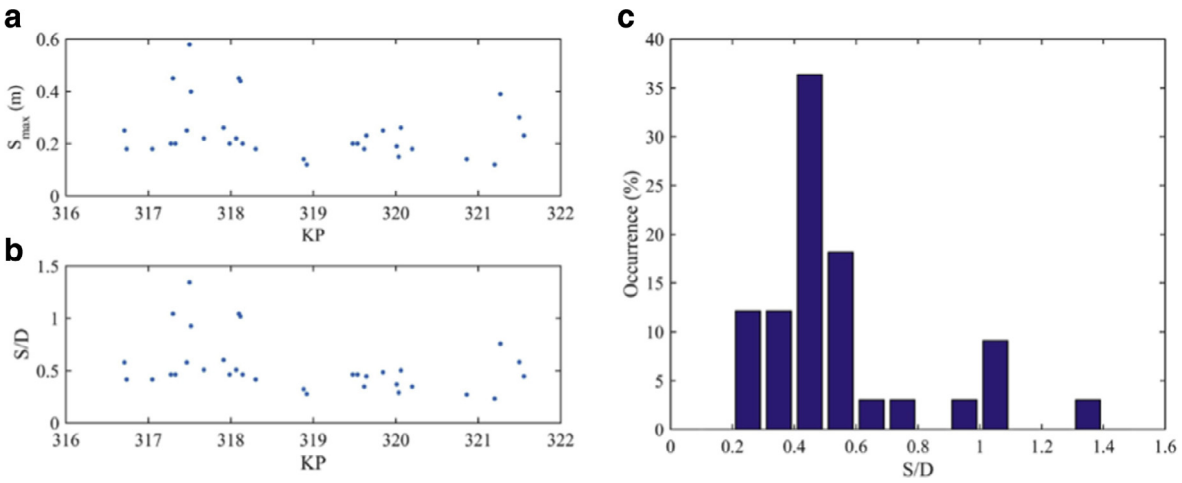

Fig. 3. (a) Maximum span depths, S_{max}, plotted against Kilometre Point, KP. The increase in KP indicates the proximity to the Northern Tasmanian coast. (b) Maximum span depths normalised over external pipe diameter. (c) Histogram of maximum span depths detected along the 5 km stretch of the surveyed pipe length.

was derived. The equation for the trend lines was assumed to be a function of θ_∞ and *S/D*, and was calculated via:

$$\theta_{max} = \frac{\tau_{max}}{(\rho_S - \rho)gd_{50}} = \left(\left[\frac{\kappa U_0}{\ln(z/z_0)} \right]^2 \times \frac{1}{\left(\frac{\rho_S}{\rho} - 1\right)gd_{50}} \right)^{C_1} \times \left(\frac{S}{D}\right)^{C_2} \quad (15)$$

where by κ is von Kármán's constant, which equates to 0.40 [22]; U_0 is the far field current velocity measured at an elevation, z, from the seabed; z_0 is the bed roughness length; ρ_s is sediment density; ρ is fluid density; g is gravitational acceleration; d_{50} is the mean sediment grain size; *S/D* is a user-defined span-depth-to-pipe-diameter ratio; and, C_1 and C_2 are constants. The exponents, C_1 and C_2, were iteratively solved using unconstrained nonlinear optimisation (see Lagarias et al. [48] for further details). The optimisation process involved the exponents being initially assumed to be 1. The differences between the data computed via CFD and the values calculated using Eq. (15) were then squared, and a scalar objective function was employed to compute the values for C_1 and C_2 that would result in the smallest difference, resembling the 'least squares' approach.

4. Results

4.1. Field observations

A field survey was conducted for the southernmost 5 km section of the Tasmanian Gas Pipeline (TGP), as per the pipeline operator's request. Further inspection was not conducted due to logistical challenges. Significant free spanning was observed from the video footage obtained via the Remotely Operated Vehicle (ROV) (Fig. 1c), and acoustic backscatter images obtained using the Autonomous Underwater Vehicle (AUV). ROV footage such as that presented in Fig. 1c suggests that the TGP had significant span depths and span lengths, and was covered in marine growth. The span depth, S, appears to be relatively small as compared to the pipe diameter, D (i.e. approximately equal to or less than $0.3D$). The sandy seabed also appeared to be relatively flat.

As only visual observations can be made from the ROV footage, the AUV was used to produce acoustic backscatter images to identify and geo-reference free spans, and subsequently, estimate the maximum free span depths. Fig. 3a reveals the maximum span depths, S, along the 5 km stretch of the TGP. KP is Kilometre Point, where an increase in KP is proportional to the proximity to the Northern Tasmanian coast. This indicated multiple incidences of free spans along this relatively short stretch of the TGP. Fig. 3b presents the same dataset normalised over the external pipe diameter, D, which is not constant along this 5 km stretch. Fig 3c shows the histogram of maximum span depths detected along the surveyed pipe length. The data revealed that over the 5 km stretch of the TGP, more than 12% of the spans had maximum *S/D* ratios smaller than 0.3.

In addition to the pipeline inspection, sediment samples were also collected within safe distances from the TGP (Fig. 1b), as recommended by the pipeline operator. Fig. 4 presents the particle size distribution for each sediment sample, which was produced by measuring the mass of sediment in each sieve. The sample number corresponds to the order of collection as shown in Fig. 1b. Due to logistical challenges only four sediment samples were obtained successfully. The sieve size corresponding to 50% passing can be observed from Fig. 4. This can be related to the mean particle size for the individual sample. By taking the average of the sieve size at 50% passing for all samples, the mean particle size, d_{50}, was estimated to be approximately 0.257 mm.

4.2. Verification and validation results

A grid independence study was performed to investigate the influence of grid refinement around the pipe and the seabed on the variables of interest. Fig. 5 suggests that the

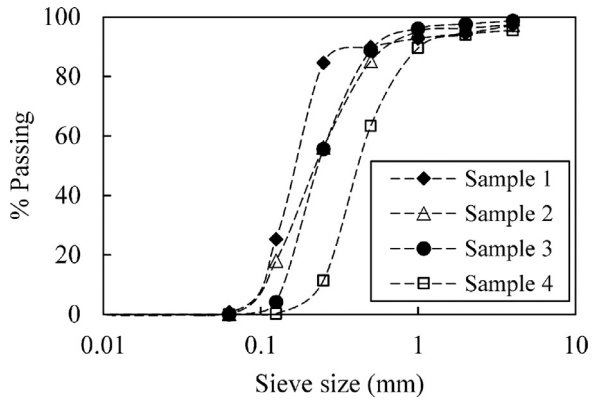

Fig. 4. Particle size distribution of marine sediment samples collected at the locations illustrated in Fig. 1b.

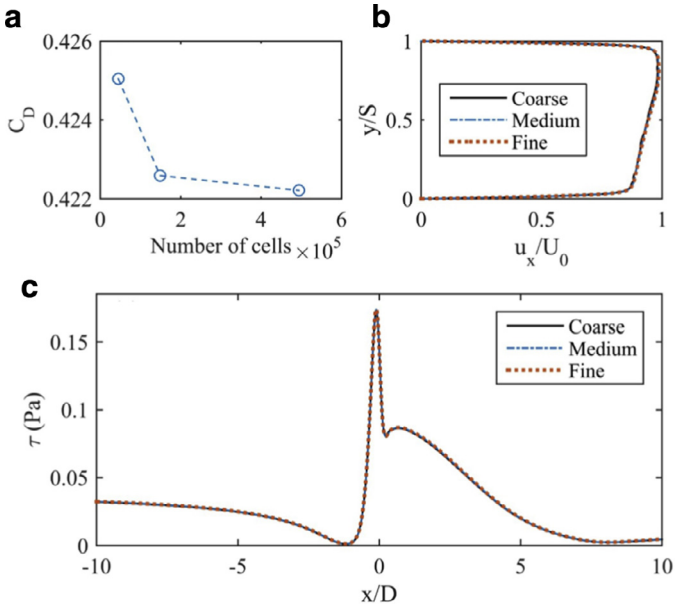

Fig. 5. Grid independence study: (a) drag coefficient for the pipe versus number of cells in the domain; (b) elevation from the seabed, y, normalised over span depth, S; plotted against mean local stream-wise velocities in the x-direction, u_x, normalised over inlet velocity, U_0, for different grid densities; (c) bed shear stress, τ, distributions along the seabed computed via different grid resolutions.

changes in the pipe's drag coefficient, C_D, local flow velocity profile beneath the pipe and bed shear stresses along the seabed were minimal, even with a grid refinement ratio of 3.32. As seen in Fig. 5a, C_D decreased by 0.58% and then by 0.09%, due to an increase in number of cells around the pipe and the seabed. With reference to Fig. 5b, the maximum stream-wise velocity beneath the pipe, u_x, increased by 0.48% and then by 0.00% with grid refinement. The maximum bed shear stress beneath the pipe, τ_{max}, only increased by 0.90%, and subsequently, by 0.16% with further refinement of the grid (Fig. 5c). Thus, by adopting τ_{max} as the main variable of interest, the resulting numerical uncertainty was estimated to be 0.35%, as the 'medium' refinement level was used for

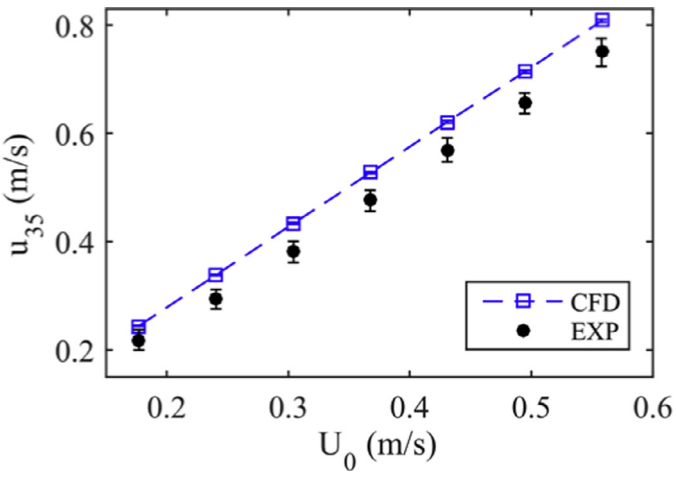

Fig. 6. Computed and measured velocity beneath the pipe at 0.035 m from the bottom plate, u_{35}, plotted against the inflow free stream velocity, U_0, at an $S=0.1$ m, corresponding to $S=D/3$, where $D=0.3$ m.

the remaining CFD simulations. The process of estimating the numerical uncertainty is presented in Section 3.3.2.

Fig. 6 presents the CFD and Circulating Water Channel (CWC) experimental results at $S=D/3$, comparing the stream-wise velocities measured at 0.035 m above the seabed, u_{35}. The error bars for the CFD data were plotted based on the numerical uncertainty, which was estimated to be 0.35%. The standard deviation was used to plot the error bars associated with the CWC experimental data. The mean difference between the CFD and experimental data was approximately 11.1%. This is larger than the validation uncertainty, U_V, of approximately 1.1%, whereby the experimental uncertainty was assumed to be 1%, which is the accuracy of the ADV [31]. The potential reasons for this discrepancy are discussed in Section 5.

Further assessment of the accuracy of the CFD model was performed by modelling the experimental setup of Jensen et al. [33]. This was done to further support the assumption that a steady-state solution is sufficient for modelling flow around a pipe close to the flat bed. Fig. 7 presents the mean velocities computed via RANS, which were superimposed on the measurements extracted from Jensen et al. [33]. The results display a good agreement at $Re=6\times10^3$. This correlation between numerical and experimental data resembled that of Akoz and Kirkgoz [15], who reported that the SST k–ω model is adequate for modelling flow around a wall-mounted circular cylinder. The mean difference between the computed velocities and measurements from Jensen et al. [33] is 4.6%. As the experimental uncertainty was not reported in Jensen et al. [33], it was not possible to confirm that validation has been achieved. However, the good qualitative agreement between the computed and measured velocity profiles are worth noting.

4.3. Full-scale numerical results

Upon attaining a high level of confidence in the numerical setup, the simulations corresponding to the conditions in

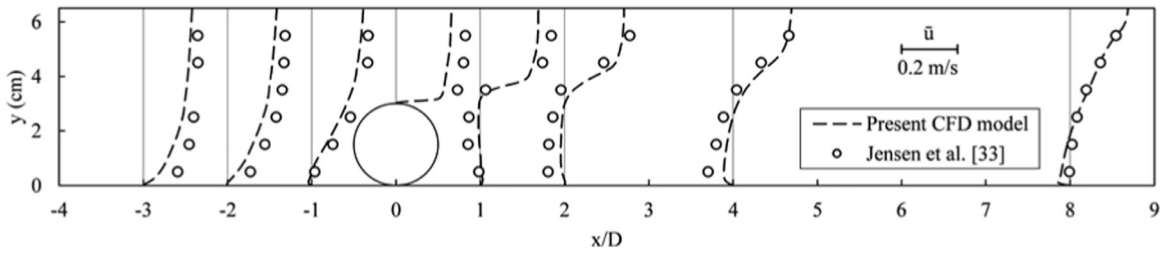

Fig. 7. Comparing mean stream-wise velocities in the x-direction computed using the present CFD model with measurements extracted from Jensen et al. [33] for $Re = 6 \times 10^3$.

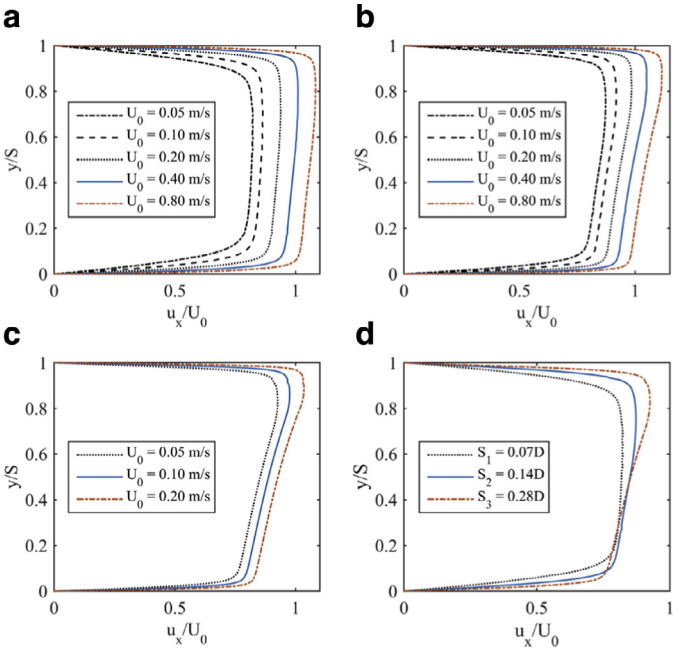

Fig. 8. (a) Elevation from the seabed, y, normalised over span depth, S; plotted against mean local stream-wise velocities in the x-direction, u_x, normalised over inlet velocity, U_0, where $S/D = 0.07$. (b) $S/D = 0.14$. (c) $S/D = 0.28$. (d) $U_0 = 0.05$ m/s.

Table 3 were performed to predict the occurrence of scour beneath the TGP. Fig. 8a shows the stream-wise velocity, u_x, normalised by inlet velocity, U_0, with reference to the elevation from the seabed, y, normalised over the span depth, S, for $S/D = 0.07$ and $0.05\,\text{m/s} \leq U_0 \leq 0.80\,\text{m/s}$. Fig. 8b shows the velocity profiles for $S/D = 0.14$, while Fig. 8c shows the plots for $S/D = 0.28$. It can be seen that the flow beneath the pipe is further accelerated as U_0 increased. With reference to Fig. 8d, it seems that even at a constant U_0 of 0.05 m/s, when S/D increases, the flow no longer resembles flow between two flat plates and becomes increasingly asymmetrical about $y/S = 0.5$. The results of cases involving higher inlet current velocities at $S/D = 0.28$ were not included, because the solutions did not converge to result in root mean squared residuals below the order of $O(10^{-4})$.

Fig. 9a presents the bed shear stress, τ, distributions along the seabed for $S/D = 0.07$. The distance along the seabed, x, is normalised over the pipe diameter, D, where the pipe is located at $x/D = 0$. The method of computing the bed shear stress is presented in Section 3.3.1. The bed shear stress distribution was seen to increase nonlinearly with an increase in the inlet velocity. Furthermore, there are highly nonlinear changes in the bed shear stresses in the vicinity of the pipe. In addition, the maximum bed shear stress appears to always occur directly beneath the pipe. Fig. 9b and c reveals a similar trend for $S/D = 0.14$ and $S/D = 0.28$, respectively. Fig. 9d compares the influence of S/D on the bed shear stress distribution, at a constant inlet velocity of $U_0 = 0.05$ m/s. Although the undisturbed bed shear stresses were the same, the maximum bed shear stress decreased as S/D increased.

The effects of the bed and pipe surface roughness lengths on the bed shear stresses were briefly investigated. Fig. 10a shows the bed shear stress distributions along the seabed for several bed roughness lengths, z_b; where $S/D = 0.14$ and $U_0 = 0.1$ m/s. The differences in the datasets were hardly noticeable. Fig. 10b shows the change in maximum bed shear stress beneath the pipe, $\Delta\tau_{max}$, relative to τ_{max} for the largest bed roughness length. It is clear that the differences are small as they are below the order of $O(10^{-3})$. Similarly, for several pipe roughness lengths that were investigated, Fig. 10c and d also shows little difference between the bed shear stresses for different pipe roughness lengths, z_p; where $S/D = 0.14$ and $U_0 = 0.1$ m/s. The range investigated in this study includes bed roughness lengths ranging from silt to fine sand [38], and pipe roughness lengths ranging from painted steel pipes to un-coated steel pipes [39]. These roughness lengths were also selected for numerical stability, as the bed roughness length should be smaller than the cell height at the bed and pipe boundaries [40].

Fig. 11a shows the maximum bed shear stress beneath the pipe, τ_{max}, for all cases. Fig. 11a shows that the maximum bed shear stress increases nonlinearly with the far field velocity, U_0, but decreases with an increase in S/D. Fig. 11b shows the bed shear stress amplification factor in the form of the Shields parameter, plotted against the far field current velocity, U_0. The bed shear stress amplification factor, τ_{max}/τ_∞, has been a variable of interest in previous studies [19,20] and hence was investigated in this paper as well. This amplification factor was seen to decrease nonlinearly with U_0, which was contrary to the nonlinear increase in maximum bed shear stress with increasing U_0 (Fig. 11a). However, the amplification factor was also seen to decrease with an increase in S/D, when U_0 remained constant.

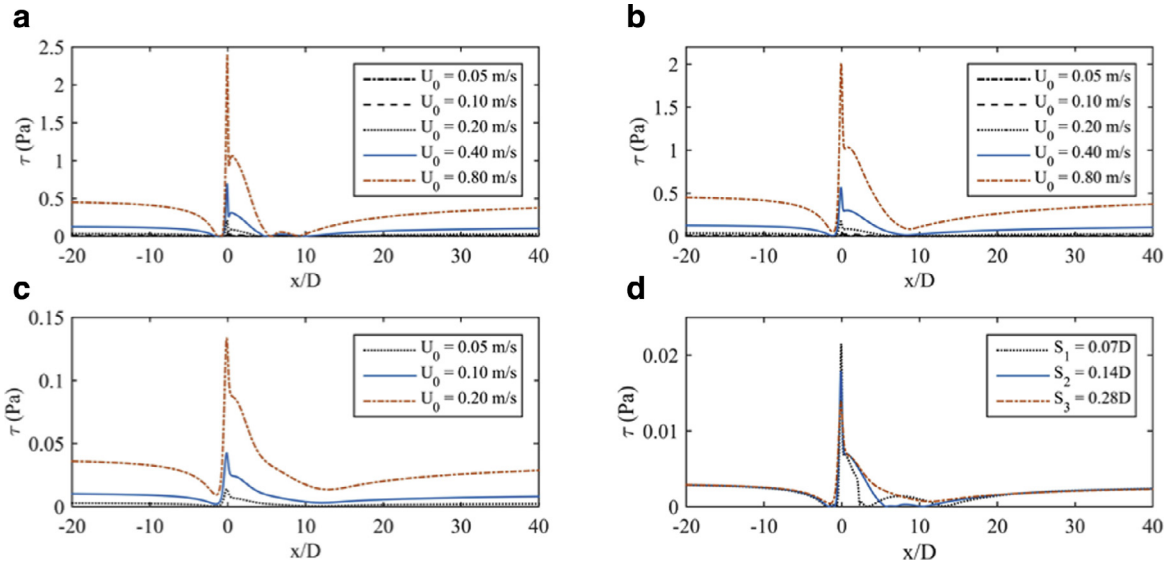

Fig. 9. (a) Bed shear stress, τ, distributions along the seabed for $S/D = 0.07$. The distance along the seabed, x, is normalised over the pipe diameter, D, where the pipe is located at $x/D = 0$. (b) $S/D = 0.14$. (c) $S/D = 0.28$. (d) $U_0 = 0.05$ m/s.

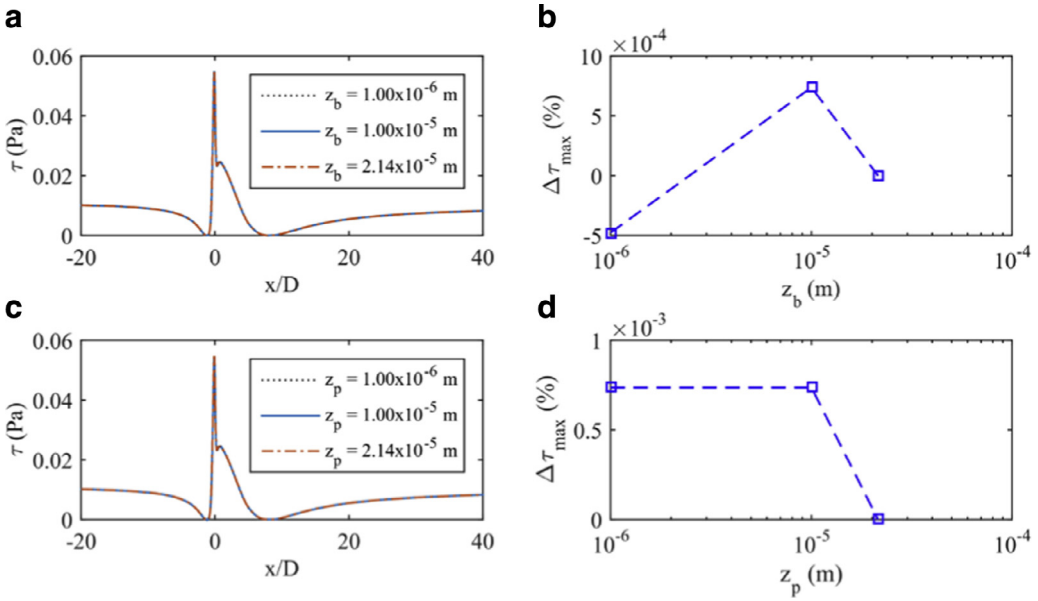

Fig. 10. (a) Bed shear stress distributions along the seabed for different bed roughness lengths, z_b; $S/D = 0.14$, and $U_0 = 0.1$ m/s. (b) Relative difference in maximum bed shear stress beneath the pipe, $\Delta\tau_{max}$, versus z_b. (c) Bed shear stress distributions along the seabed for different pipe roughness lengths, z_p; $S/D = 0.14$, and $U_0 = 0.1$ m/s. (d) $\Delta\tau_{max}$ versus z_p.

Fig. 12a presents the maximum Shields parameter, θ_{max}, plotted against the far field current velocity, U_0, at different S/D ratios. Based on the mean grain size (estimated via Fig. 4), the critical Shields parameter (i.e. $\theta_{cr} = 0.048$) was obtained from Barton et al. [23] and plotted as the red horizontal line. When $\theta_{max} > \theta_{cr}$, then scour beneath the TGP is likely to occur. With reference to Fig. 12a, $\theta_{max} > \theta_{cr}$ when $U_0 = 0.2$ m/s and $S/D = 0.07$. This occurred at a low current velocity, which is below that of the maximum eastward horizontal flow velocity of 0.32 m/s, and maximum northward velocity of 0.21 m/s recorded by the ADCP. Similar to the maximum bed shear stress beneath the pipe (Fig. 11a), the maximum Shields parameter increases nonlinearly with the increase in U_0, while it decreases with an increase in S/D.

In Fig. 12b, the far field current velocity, U_0, is converted to the undisturbed Shields parameter, θ_∞, using Eq. (14). θ_{max} was plotted against θ_∞ with logarithmic axes, and similar to Fig. 12a, the red horizontal line represents the critical Shields parameter. The trend lines were plotted with an assumed power law relationship, where the exponents in Eq. (15) were iteratively solved using unconstrained nonlinear optimisation (see Section 3.4 for further details). The result of the optimisation process was the converged values of the exponents (i.e. $C_1 = 0.864$ and $C_2 = -0.333$). Hence, Eq. (15) can be written

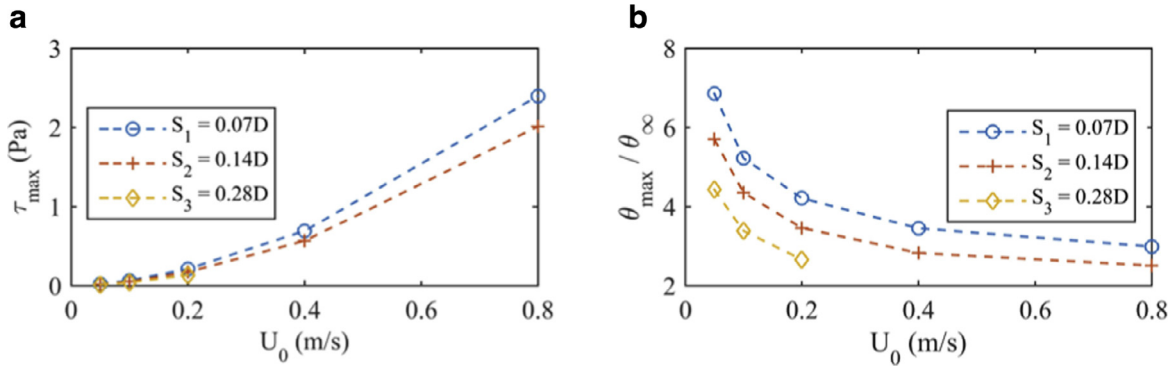

Fig. 11. (a) Maximum bed shear stress beneath the pipe, τ_{max}, plotted against inlet velocity, U_0. (b) Maximum Shields parameter normalised over far field Shields parameter, $\theta_{max}/\theta_\infty$, plotted against U_0.

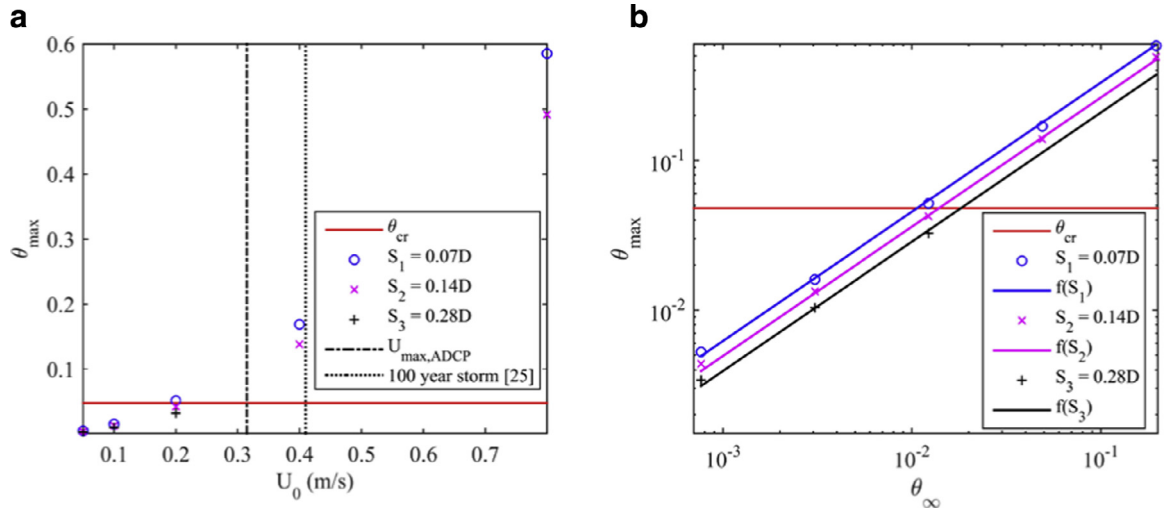

Fig. 12. (a) Maximum Shields parameter beneath the pipe, θ_{max}, versus far field velocity, U_0, at several *S/D* ratios. (b) θ_{max} versus undisturbed Shields parameter, θ_∞. The trend lines were plotted using Eq. (16), where $R^2 = 0.9986$.

as:

$$\theta_{max} = \frac{\tau_{max}}{(\rho_S - \rho)gd_{50}} = \left(\left[\frac{\kappa U_0}{\ln(z/z_0)}\right]^2 \times \frac{1}{\left(\frac{\rho_S}{\rho} - 1\right)gd_{50}}\right)^{0.864} \times \left(\frac{S}{D}\right)^{-0.333} \quad (16)$$

With reference to the CFD data, Eq. (16) corresponded to a squared correlation coefficient, R^2 of 0.9986. The good fit can be observed in Fig. 12b, as more than 99% of the total variation of the CFD data can be reproduced via Eq. (16).

5. Discussion

The field investigation provided an insight into the number of spans and span depths along the TGP, far field ensemble-averaged velocities and mean sediment grain size in the vicinity of the surveyed area. A significant amount of free spanning was observed along the 5 km stretch of the surveyed area (Fig. 3a and b). In addition, more than 12% of detected spans have maximum *S/D* ratios smaller than 0.3 (Fig. 3c). Thus, a significant amount of small span depths can be expected along the TGP, considering the fact that the TGP is over 300 km long. Therefore, it will be beneficial to be able to predict whether scour will occur beneath the TGP in areas with small span depths.

In addition, as the seabed appeared to be relatively flat in Fig. 1c, a flat boundary was used to represent the seabed in the CFD simulations for simplicity. The seabed topography along the path at which the TGP was laid was also reported to be relatively featureless [25]. Although there appears to be a significant amount of marine growth on the TGP (Fig. 1c), previous experimental investigations on pipe roughness, representing marine growth, indicate that it poses an insignificant influence on the scour process [1]. Thus, the effects of hard and soft marine growth on the pipe were not included in the scope of this work.

The mean particle size, d_{50}, was estimated to be approximately 0.257 mm, based on the particle size distributions (Fig. 4). Therefore, it was assumed that the sediment in the surveyed area is mainly comprised of non-cohesive medium sand [23], which is in agreement with the range reported in [25]. The sediment in the Bass Strait, in the vicinity of the TGP, was previously reported to be primarily comprised of fine and medium grained quartzose sands [25]. Interestingly, the particle size distribution was seen to slightly shift towards

the right as the sample number increases. With reference to the sampling locations (Fig. 1b), this suggests that the sediment closer to the shore are generally smaller in size. However, this would only be true for the surveyed area.

With regards to the grid independence study, the numerical results computed with a 'medium' mesh (i.e. 400 grid points on the pipe) were deemed to be grid-independent, as the changes in the results due to grid refinement are very small (Fig. 5). As for the comparison between the CFD and CWC results (Fig. 6), validation was not achieved as the discrepancies between the CFD and experimental data, E, exceeded the validation uncertainty, U_V [44]. The difference between the datasets is hypothesised to stem from: (1) the combined effects of modelling uncertainties (e.g. boundary conditions, turbulence model, fluid properties, etc. [44]), in addition to the numerical uncertainties; and, (2) the pressure field generated by the strut that was used to hold the ADV in the CWC (Fig. 2), which was not modelled in the CFD simulations. Nevertheless, both CFD and CWC results have a similar gradient, especially at higher inlet velocities. The simulation setup was still deemed to be reliable as there is a good agreement between the CFD and experimental data in Fig. 7, in conjunction with a very small numerical uncertainty.

Full-scale CFD computations were performed upon establishing a reliable numerical model. From Fig. 8, it can be seen that dimensionless flow velocity beneath the pipe, u_x/U_0, increases when U_0 increases at a constant S/D. The flow beneath the pipe is further accelerated as U_0 increased, which suggests a nonlinear increase in the bed shear stresses beneath the pipe, as $\tau = \rho u_*^2$ [22]. This nonlinear increase in bed shear stress due to an increase in U_0 is reflected in Fig. 9. With reference to Fig. 8a, a symmetrical flow pattern is observed at a low U_0. However, as U_0 increases, the velocities at the upper region of the velocity profile (i.e. the region closer to the pipe) become higher relative to the velocities near the seabed. This can be attributed to two occurrences as the flow becomes increasingly turbulent: (1) the viscous region of the boundary layer attached to the pipe's surface decreases in thickness; and, (2) flow separation on the pipe's bottom surface is delayed, pushing the separation point further downstream [49]. A similar situation is observed in Fig. 8b and c.

There are highly nonlinear changes in the bed shear stresses in the vicinity of the pipe (Fig. 9), suggesting that the presence of the pipe poses a significant influence on the bed shear stresses. The fact that the maximum bed shear stress appears to always occur beneath the pipe, implies that the likelihood of scour occurring is maximum at the point beneath the pipe. These bed shear stress distributions are in good agreement with the shear distributions presented in Ong et al. [17], who analysed the applicability of the k–ε turbulence model for different Reynolds numbers, but did not focus on the scour process underneath the pipe. Fig. 9d shows that although the undisturbed bed shear stresses were the same, the maximum bed shear stress decreased as S/D increased, indicating that the likelihood of scour occurring decreases with an increase in S/D.

The maximum bed shear stress beneath the pipe, τ_{max}, was seen to increase nonlinearly with U_0, but decrease with an increase in S/D (Fig. 11a). This suggests that the capacity for scour increases with the increase in U_0, and with decreasing S/D. Griffiths et al. [19] reported that the amplification factor decreases with an increase in the span depth, which agrees with Fig. 11b. This occurrence can be attributed to the decrease in maximum bed shear stress beneath the pipe as S/D increases, while the undisturbed bed shear stress remains constant due to a constant U_0. As the Shields parameter is a dimensionless form of the bed shear stress, an increase in S/D with a constant U_0 also results in a decrease in θ_{max}, and subsequently, a decrease in the amplification factor. However, Fig. 11b shows that the amplification factor is also a function of the far field current velocity, U_0, where it decreases nonlinearly with U_0. This was not discussed by Griffiths et al. [19]. Nevertheless, the shear stress amplification approach does not offer a direct relationship to the occurrence of scour. Therefore, this study focused on predicting the maximum Shields parameter beneath the TGP under steady currents, where it can be compared to the critical Shields parameter for the mean sediment grain size.

Fig. 12a shows that even at a small U_0, which is below the maximum flow velocity recorded by the ADCP, the maximum Shields parameter beneath the TGP has exceeded the critical Shields parameter. Thus, the occurrence of scour beneath the TGP in areas with small span depths (i.e. $S/D < 0.3$) can be expected, due to the fact that flow velocities as high as 0.32 m/s were recorded. At higher current velocities (e.g. during a storm event), the occurrence of scour beneath the TGP will likely be more severe. These findings can be related to the significant amount of free spanning that was observed along the 5 km stretch of the surveyed area (Fig. 3a and b). Overall, the Shields parameter approach appears to be a more reliable method for scour prediction, as compared to using the shear stress amplification factor.

The high squared correlation coefficient, R^2, of 0.9986 implies that Eq. (16) can be used, with high confidence, to calculate the maximum Shields parameter beneath the TGP in areas with a small S/D under steady currents. Eq. (16) is valid for $S/D < 0.3$, where there is no periodic vortex shedding in the wake of the pipe [5,8], and the friction velocity beneath the pipe is constant over time [16,17]. Hence, $S/D = 0.28$ was selected as the upper limit because the presence of periodic vortex shedding at higher span depths could produce different results. Nevertheless, $S/D < 0.3$ is of interest not only because the capacity for scour is higher at smaller span depths, but also, performing rectification works such as installing grout bags are often impractical. The additional option to conduct inexpensive RANS-based CFD simulations to modify Eq. (16) is also available.

6. Conclusions

A combination of numerical, experimental and field work was undertaken to predict the occurrence of scour beneath the Tasmanian Gas Pipeline (TGP) in areas with existing

small span depths under steady currents. Full-scale 2D CFD computations were performed by incorporating information attained through field measurements. A good agreement between model-scale CFD data and experiments was demonstrated. A range of *S/D* ratios and steady current velocities, U_0, were considered in the numerical simulations. A trend line equation was fitted to the full-scale CFD data using unconstrained nonlinear optimisation, which resulted in a very high correlation coefficient. The following conclusions can be drawn from this work:

- A significant occurrence of spans with small maximum span depths (i.e. $S/D < 0.3$) were detected during the field survey; thus, supporting the need to develop an equation to predict whether scour will occur under these circumstances.
- The maximum bed shear stress beneath the pipe increases nonlinearly with U_0, but decreases with an increase in *S/D*. Hence, the capacity for scour increases with an increase in U_0, but decreases with an increase in *S/D*.
- The shear stress amplification factor decreases nonlinearly with U_0; hence, it does not accurately reflect the occurrence of scour and it is not an appropriate tool for scour prediction.
- Eq. (16) was developed to calculate the maximum Shields parameter beneath the pipe, θ_{max}, based on the undisturbed Shields parameter, θ_∞, and *S/D;* θ_{max} can be compared to the critical Shields parameter, θ_{cr}, for the particular sediment grain size. Eq. (16) can be used to predict the occurrence of scour beneath the TGP in areas with a small *S/D* under steady currents. Eq. (16) is valid for $S/D < 0.3$, where there is no periodic vortex shedding in the wake of the pipe [5,8], and the bed shear stress beneath the pipe is constant over time [16,17].
- High horizontal flow velocities recorded by the Acoustic Doppler Current Profiler suggest that the occurrence of scour beneath the TGP is highly likely, based on the maximum Shields parameter computed via CFD.

The long-term goal is to better understand all parameters that play a role in inducing scour beneath pipelines with existing small span depths. For instance, investigating the influence of various pipe diameters and having a deformable seabed are work in progress.

Acknowledgments

The authors wish to thank Barry Parsons from Tasmanian Gas Pipeline Pty. Ltd., and Andrew Hargrave from Adetra Pty Ltd for funding and authorising this research project. The generous assistance and advice from Fauzi Hardjanto, Vanessa Lucieer, Karl Manzer, Nathan Kemp, Isak Bowden-Floyd, Shuhong Chai, Michael Underhill, Alan Faulkner, Christopher Coppard, Supun Randeni and the Dell Richey II fishing vessel crew in obtaining field measurements and conducting laboratory experiments are greatly appreciated. The corresponding author also gratefully acknowledges the Australian Maritime College and Tasmanian Partnership for Advanced Computing for providing access to their high performance computing facilities.

References

[1] B.M. Sumer, J. Fredsøe, The Mechanics of Scour in the Marine Environment, World Scientific, Singapore, 2002.
[2] D. Liang, L. Cheng, K. Yeow, Ocean Eng. 32 (13) (2005) 1590–1607.
[3] M. Drago, M. Mattioli, R. Bruschi, L. Vitali, Philos. Trans. R. Soc. London, Ser. A 373 (2033) (2015) 20140111.
[4] Y.M. Chiew, J. Hydraul. Eng. 116 (4) (1990) 515–529.
[5] Y. Mao, The Interaction between a Pipeline and an Erodible Bed (Ph.D. Thesis). Lyngby, Denmark: Technical University of Denmark; 1986.
[6] B.M. Sumer, C. Truelsen, T. Sichmann, J. Fredsøe, Coastal Eng. 42 (4) (2001) 313–335.
[7] Q. Zhang, S. Draper, L. Cheng, H. An, Coast. Eng. 116 (2016) 103–117.
[8] P.W. Bearman, M.M. Zdravkovich, J. Fluid Mech. 89 (1) (1978) 33–47.
[9] S.A. Hughes, Physical Models and Laboratory Techniques in Coastal Engineering, World Scientific, 1993.
[10] G. Masselink, M.G. Hughes, Introduction to Coastal Processes and Geomorphology, Hodder Arnold, London, 2003.
[11] H. Mohr, S. Draper, L. Cheng, D. White, Coastal Eng. 110 (2016) 111–126.
[12] J. Fredsøe, B. Sumer, M. Arnskov, Int. J. Offshore Polar Eng. 2 (1) (1992).
[13] S.H. Leckie, S. Draper, D.J. White, L. Cheng, A. Fogliani, Coastal Eng. 95 (2015) 130–146.
[14] M. Abrahamsen Prsic, M.C. Ong, B. Pettersen, D. Myrhaug, Mar. Struct. 46 (2016) 127–148.
[15] M.S. Akoz, M.S. Kirkgoz, Trans. Can. Soc. Mech. Eng. 33 (2) (2009) 189–215.
[16] M.C. Ong, T. Utnes, L.E. Holmedal, D. Myrhaug, B. Pettersen, Coastal Eng. 57 (10) (2010) 931–947.
[17] M.C. Ong, T. Utnes, L.E. Holmedal, D. Myrhaug, B. Pettersen, J. Offshore Mech. Arct. Eng. 134 (021803) (2012) 1–11.
[18] M. Zhao, L. Cheng, B. Teng, J. Waterw. Port Coastal Ocean Eng. 133 (4) (2007) 286–295.
[19] T. Griffiths, F. Zhao, M. Kalkhoven, W. Shen, M. Xu, Z. Zan, et al., in: Proceedings of the Seventh International Conference on Scour and Erosion, Perth, Australia, 2-4 December 2014, CRC Press, 2014, p. 317.
[20] W. Shen, T. Griffiths, M. Xu, J Leggoe, in: ASME 2013 Thirty-Second International Conference on Ocean, Offshore and Arctic Engineering: American Society of Mechanical Engineers, 2013 p. V04ATA048-V04AT04A.
[21] Shields A, Anwendung der Aehnlichkeitsmechanik und der Turbulenzforschung auf die Geschiebebewegung (Dissertation Doktor-Ingenieur). Berlin: Preussischen Versuchsanstalt für Wasserbau; 1936.
[22] R. Soulsby, Dynamics of Marine Sands: a Manual for Practical Applications, Thomas Telford, 1997.
[23] G.J. Barton, R.R. McDonald, J.M. Nelson, R.L. Dinehart, Simulation of Flow and Sediment Mobility Using a Multidimensional Flow Model for the White Sturgeon Critical-Habitat Reach, Kootenai River near Bonners Ferry, Idaho, Geological Survey, 2005 Scientific Investigations Report 2005-5230. Virginia: U.S.
[24] Z. Zang, L. Cheng, M. Zhao, D. Liang, B. Teng, Coastal Eng. 56 (4) (2009) 458–466.
[25] OSDAS. Environment Plan (EP) Summary. Perth, Australia: National Offshore Petroleum Safety and Environmental Management Authority; 2014. p. 50.
[26] Teledyne RD Instruments, Sentinel V Self-Contained 20 m, 50 m, 100 m Profiling ADCP, 2011 Poway, California.
[27] C. Gostnell, J. Yoos, Hydrogr. J. 118 (2005) 17.
[28] J. McInerney, A.L. Forrest, J.Y. Lee, F. Hardjanto, R. Cossu, Scour Propagation Beneath a Subsea Pipeline in High and Low Energy Environments, OCEANS 16 Monterey, Monterey, California, 2016.

[29] I.F. Akyildiz, D. Pompili, T. Melodia, Ad hoc Netw. 3 (3) (2005) 257–279.
[30] R. Panish, M. Taylor, Achieving High Navigation Accuracy Using Inertial Navigation Systems in Autonomous Underwater Vehicles, IEEE, 2011, pp. 1–7. OCEANS 2011 IEEE-Spain.
[31] SonTek/YSI, SonTek/YSI ADVField/Hydra Acoustic Doppler Velocimeter (Field), 2001 Technical Documentation, San Diego, California.
[32] G. Voulgaris, J.H. Trowbridge, J. Atmos. Ocean Technol. 15 (1) (1998) 272–289.
[33] B.L. Jensen, B.M. Sumer, H.R. Jensen, J. Fredsoe, J. Offshore Mech. Arct. Eng. 112 (3) (1990) 206–213.
[34] J. Tu, G.H. Yeoh, C. Liu, Computational Fluid Dynamics: A Practical Approach, first ed., Butterworth-Heinemann, Oxford, 2008.
[35] F.R. Menter, AIAA J. 32 (8) (1994) 1598–1605.
[36] ITTC, in: International Towing Tank Conference: Recommended Procedures and Guidelines, 2011.
[37] R. Soulsby, J. Humphery, Water Wave Kinematics, Springer, 1990, pp. 413–428.
[38] Det Norske Veritas, Recommended Practice DNV-RP-E305: On-Bottom Stability Design of Submarine Pipelines, Oslo, Norway, 1988.
[39] Det Norske Veritas, Recommended Practice DNV-RP-F105: Free Spanning Pipelines, Høvik, Norway, 2006.
[40] CD-adapco. User Guide STAR-CCM+ Version 10.02. 2015.
[41] International Towing Tank Conference, Uncertainty Analysis in CFD Verification and Validation Methodology and Procedures. ITTC – Recommended Procedures and Guidelines, 2008.
[42] Y. Jin, J. Duffy, S. Chai, C. Chin, N. Bose, Ocean Eng. 118 (2016) 93–106.
[43] C.D. Simonsen, J.F. Otzen, C. Klimt, N.L. Larsen, F Stern, in: Twenty-Ninth Symposium on Naval Hydrodynamics, 2012, pp. 26–31.
[44] F. Stern, R.V. Wilson, H.W. Coleman, E.G. Paterson, J. Fluids Eng. 123 (4) (2001) 793–802.
[45] R.V. Wilson, F. Stern, H.W. Coleman, E.G. Paterson, J. Fluids Eng. 123 (4) (2001) 803–810.
[46] E.A Hansen, in: Proceedings of the International Conference on Offshore Mechanics and Arctic Engineering: American Society of Mechanical Engineers, 1992, p. 133.
[47] B.M. Sumer, R.J. Whitehouse, A. Tørum, Coastal Eng. 44 (2) (2001) 153–190.
[48] J.C. Lagarias, J.A. Reeds, M.H. Wright, P.E. Wright, SIAM J. Optim. 9 (1) (1998) 112–147.
[49] F.M. White, Fluid Mechanics, seventh ed., McGraw-Hill, New York, 2011.